

An End-to-End Deep Learning Histochemical Scoring System for Breast Cancer TMA

Jingxin Liu, Bolei Xu, Chi Zheng, Yuanhao Gong, Jon Garibaldi, Daniele Soria, Andrew Green, Ian O. Ellis, Wenbin Zou, Guoping Qiu

Abstract—One of the methods for stratifying different molecular classes of breast cancer is the Nottingham Prognostic Index Plus (NPI+) which uses breast cancer relevant biomarkers to stain tumour tissues prepared on tissue microarray (TMA). To determine the molecular class of the tumour, pathologists will have to manually mark the nuclei activity biomarkers through a microscope and use a semi-quantitative assessment method to assign a histochemical score (H-Score) to each TMA core. Manually marking positively stained nuclei is a time consuming, imprecise and subjective process which will lead to inter-observer and intra-observer discrepancies. In this paper, we present an end-to-end deep learning system which directly predicts the H-Score automatically. Our system imitates the pathologists' decision process and uses one fully convolutional network (FCN) to extract all nuclei region (tumour and non-tumour), a second FCN to extract tumour nuclei region, and a multi-column convolutional neural network which takes the outputs of the first two FCNs and the stain intensity description image as input and acts as the high-level decision making mechanism to directly output the H-Score of the input TMA image. To the best of our knowledge, this is the first end-to-end system that takes a TMA image as input and directly outputs a clinical score. We will present experimental results which demonstrate that the H-Scores predicted by our model have very high and statistically significant correlation with experienced pathologists' scores and that the H-Score discrepancy between our algorithm and the pathologists is on par with the inter-subject discrepancy between the pathologists.

Index Terms—H-Score, Immunohistochemistry, Diaminobenzidine, Convolutional Neural Network, Breast Cancer

1 INTRODUCTION

Breast cancer (BC) is a heterogeneous group of tumours with varied genotype and phenotype features [1]. Recent research of Gene Expression Profiling (GEP) suggests that BC can be divided into distinct molecular tumour groups [2]. Personalised BC management often utilizes robust commonplace technology such as immunohistochemistry (IHC) for tumour molecular profiling [3].

Diaminobenzidine (DAB) based IHC techniques stain the target antigens (detected by biomarkers) with brown colouration (positive) against a blue colouration (negative) counter-stained by Hematoxylin (see Fig.1 for some example images). To determine the biological class of the tumour, pathologists will mark the nuclei activity biomarkers through a microscope and give a score based on a semi-quantitative assessment method called the modified histochemical scoring (H-Score) [4]. The H-Scores of tissue samples stained with different biomarkers are combined together to determine the biological class of a case. Clinical decision making is to choose an appropriate treatment from a number of available treatment options according to the biological class of the tumour. For instance, one of

the methods for stratifying different molecular classes is the Nottingham Prognosis Index Plus (NPI +) [1] which uses 10 breast cancer relevant biomarkers to stain tumour tissues prepared on tissue microarray (TMA). Tissue samples stained by each of these 10 biomarkers are given a histochemical score (H-Score) and these 10 scores together will determine the biological class of the case.

Therefore, H-Score is one of the most important pieces of information for molecular tumour classification. When the tumour region occupies more than 15% of the TMA section, a H-Score is calculated based on a linear combination of the percentage of strongly stained nuclei (SSN), the percentage of moderately stained nuclei (MSN) and the percentage of weakly stained nuclei (WSN) according to:

$$H - Score = 1 \times WSN + 2 \times MSN + 3 \times SSN \quad (1)$$

The final score has a numerical value ranges from 0 to 300. Thus, the histochemical assessment of the TMA's is based on the following semi-quantitative information: the total number of cells, the number of tumour cells and the stain intensity distributions within the tumour cells.

In clinical practice, diagnosis requires averaging two experienced pathologists' assessments. Manually marking the positively stained nuclei is obviously a time consuming process. As visual assessment of the TMA's is subjective, there is the problem of inter-observer discrepancy and the issue of repeatability. The semi-quantitative nature of the method (strongly stained, moderately stained and weakly stained, the definitions of strong, moderate and weak cannot be precise and subjective), makes it even more difficult to ensure inter-subject as well as intra-subject consistency.

• J. Liu, B. Xu, Y. Gong, W. Zou, and G. Qiu are with the College of Information Engineering, Shenzhen University and Guangdong Key Laboratory of Intelligent Information Processing, China; G. Qiu is also with School of Computer Science, The University of Nottingham, UK
• C. Zheng is with Ningbo Yongxin Optics Co., LTD, Zhejiang, China
• J. Garibaldi is with School of Computer Science, The University of Nottingham, UK
• D. Soria is with Department of Computer Science, The University of Westminster, UK
• A. Green and I. O. Ellis are with Faculty of Medicine & Health Sciences, The University of Nottingham, United Kingdom.

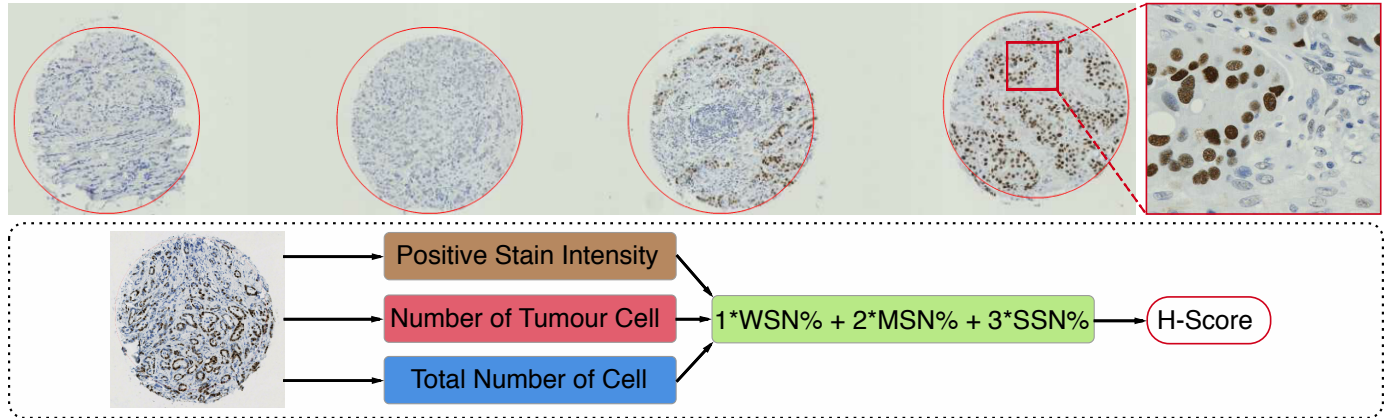


Fig. 1: Top: Example images extracted from digital TMA slides. Each red circle contains one TMA core stained by Diaminobenzidine-Hematoxylin (DAB-H). The brown colours indicate positive and the blue colours indicate negative. Bottom: A schematic illustration of the traditional manual H-Score procedure: it needs to first count the total number of nuclei, then the number of strongly stained, moderately stained and weakly stained tumour nuclei, respectively. The final H-Score is then calculated according to Eq.1.

With the increasing application of clinicopathologic prognosis, Computer Aided Diagnosis (CAD) systems have been proposed to support the pathologists' decision making. The key parameters in tissue image assessment include the number of tumour cells, the positive staining intensities within these cells and the total number of all cells in the image. To classify the positively stained pixels and their stain intensities, methods such as colour deconvolution that perform mathematical transformation of the RGB image [5] [6] are widely used to separate positive stains from negative stains. Numerous computer-assisted approaches have been proposed for cell or nuclei detection and segmentation [7]. Most literature [8], [9] on histopathology image analysis perform various low-level quantification steps, there is still little attempt to perform end-to-end assessment of the image directly.

Traditional assessment methods have at least three unsolved issues for both the pathologists and the CAD systems. Firstly, the positive staining intensity needs to be categorized into four classes: *unstained*, *weak*, *moderate*, and *strong*. However, there is no standard quantitative criterion for classifying the DAB stain intensity. Thus, two pathologists often classify the same staining intensity into two different categories or two different intensities into the same category. Furthermore, the human visual system may pay more attention to strongly stained regions but they are often surrounded by a variety of staining intensities [9], which may also affect the assessment results. Secondly, cell/nuclei instance counting is a very important parameter in the assessment. Nevertheless, both human and computer still cannot deal with the difficulty of counting overlapping cells very well. Moreover, variability in the appearance of different types of nucleus, heterogeneous staining, and the complex tissue architectures make individually segmenting cell/nuclei a very challenging problem. Thirdly, the apparent size differences between tumour nuclei and normal nuclei will affect the quantitative judgement of tumour nuclei assessment. Examples of these challenging cases are illustrated in Fig. 2.

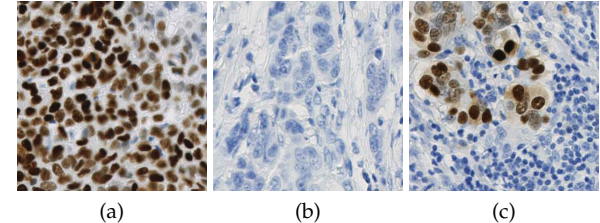


Fig. 2: Examples of challenging cases of quantitative measurement of biomarkers based on visual assessment. (a) A variety of stain intensities; (b) unclear staining and overlapping of nucleus; (c) Size differences between different type of nucleus.

In this paper, we ask this question: is it possible to develop a CAD model that would directly give a high-level assessment of a digital pathological image, just like an experienced pathologist would, for example, to give out a H-Score directly? In an attempt to answer this question, we propose an end-to-end deep learning system for directly predicting the H-Scores of breast cancer TMA images, see Fig. 3. Instead of pushing the raw digital images into the neural network directly, we follow a similar process that pathologists use for H-Score estimation. We first construct a stain intensity nuclei image (SINI) and a stain intensity tumour image (SITI), which contain all general nuclei region (tumour and non-tumour) and tumour region respectively and their corresponding stain intensity information. The SINI and SITI block irrelevant background pixels while only retain useful information for calculating the H-Score. These two H-Score relevant images are then fed into a dual-channel convolutional neural network with two input pipelines, which are finally merged into one pipeline to give an output (H-Score). The innovative characteristic of our proposed method is that it is mimicking the H-Score process of the pathologists, while without counting the total number of nuclei, the number of tumour nuclei, and categorising the tumour nuclei based on the intensity of their positive stain. To the best of our knowledge, this is a first work that attempts to develop deep learning based end-to-end TMA processing model that directly outputs the

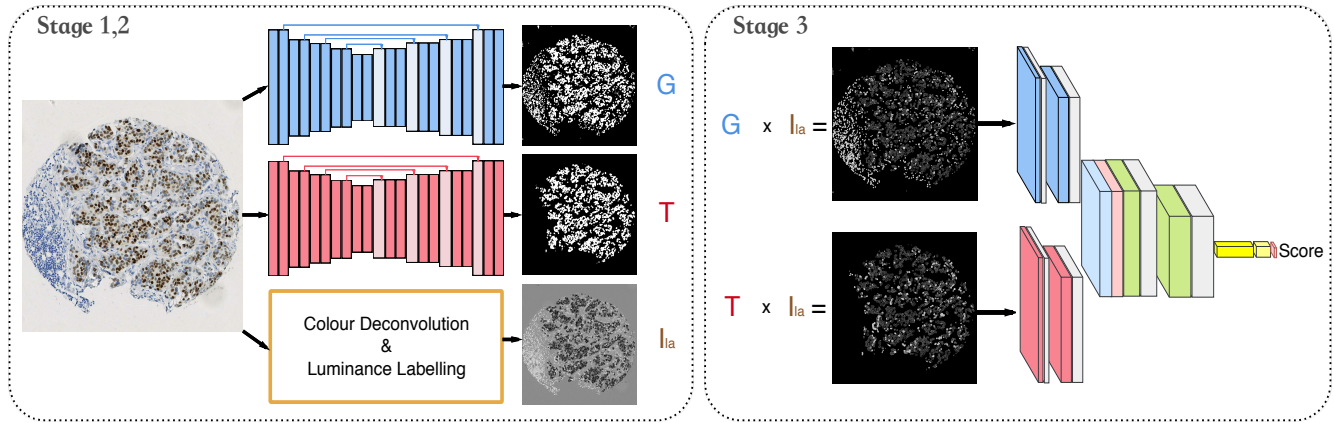


Fig. 3: The overview of our proposed H-Score prediction framework. An input TMA image is first processed by two FCNs to extract tumour cells and all cells (tumour and non-tumour) to produce two mask images. The input image is also processed by colour deconvolution and positive stain classification to output a stain intensity description image. The two mask images are used to filter out irrelevant information in the stain intensity description image and only the useful information is fed to a deep convolutional neural network for the prediction of H-Score of the input TMA.

histochemical scores. We will present experimental results which demonstrate that the H-Scores predicted by our model have high and statistically significant correlation with experienced pathologists' scores and that the H-Scoring discrepancy between our algorithm and the pathologists is on par with that between the pathologists. Although it is still perhaps a long way from clinical use, this work nevertheless demonstrates the possibility of automatically scoring cancer TMA's based on deep learning.

2 RELATED WORKS

Researchers have proposed various computer-assisted analysis methods related to histochemical score assessment. For pixel-level positive stain separation, Pham [10] adapted the Yellow channel in the CMYK model, which is believed to have strong correlation with the DAB stain. Ruifrok [5] presented the brown image calculated based on mathematical transformation of the RGB image. His later work utilized the predefined stain matrix for stain colour decomposition [6]. CAD systems have also been developed for cell nucleus segmentation. Early works employed different filters to segment cells [11], [12]. While morphology-based methods are applied in recent proposed conventional cell segmentation systems. Arslan *et al.* [13] constructed an attributed relational graph on four predefined types of cell nucleus boundaries for fluorescence images; Shu *et al.* [14] proposed utilizing morphological filtering and seeded watershed for overlapping nuclei segmentation in IHC stained histopathology images.

With the development of deep learning techniques, various deep neural network based CAD models have been published. Ronneberger *et al.* [15] proposed U-Net with symmetric U shape architecture, which have been proved have strong universality on biomedical segmentation applications [16], [17]. Deep convolutional networks with deeper architectures can be used to build more complex models which will result in more powerful solutions. Li [18] used a 88-layer residual network for simultaneously human epithelial type 2 (HEp-2) cell segmentation and classification.

AggNet with a novel aggregation layer is proposed for mitosis detection in breast cancer histology images [19]. Google brain presented a multi scale convolutional neural network (CNN) model to aid breast cancer metastasis detection in lymph nodes [20]. A deep learning-based system is proposed for the detection of metastatic cancer from whole slide images, which won the Camelyon Grand Challenge 2016 [21]. Shah *et al.* [22] presented the first completely data-driven model integrated numerous biologically salient classifiers for invasive breast cancer prognosis.

Most existing high-level CAD frameworks directly follow the assessment criteria by extracting quantitative information from the digital images. Masmoudi *et al.* [8] proposed an automatic Human Epidermal Growth Factor Receptor 2 (HER2) assessment method, which is an assemble algorithm of colour pixel classification, nuclei segmentation and cell membrane modelling. Gaussian-based bar filter was used for membrane isolation after colour decomposition in [23]. Trahearn *et al.* [9] established a two-stage registration process for IHC stained WSI scoring. Thresholds were defined for DAB stain intensity groups, and tumour region and nuclei were detected by two different detectors. Recently, Zhu [24] proposed to train an aggregation model based on deep convolutional network for patient survival status prediction.

3 METHODOLOGY

In this paper, we propose to develop a CNN based CAD framework for biomarker assessment of TMA images. Instead of using CNN as a feature extractor or for low level processing such as cell segmentation and counting, we have developed an end-to-end system which directly predicts the biomarker score (H-Score).

The overview of the H-Score prediction framework is illustrated in Fig.3. It consists of three stages: 1) general nuclei and tumour regions segmentation; 2) stain intensity description; 3)constructing the SINI and SITI, and predicting the final histochemical score (H-Score) by the Region Atten-

tion Multi-column Convolutional Neural Network (RAM-CNN).

The rationale of this architecture is as follows: as the number of nuclei, the number of tumour nuclei and the stain intensity of the tumour nuclei are the useful information for predicting H-Score, we therefore extract two region masks that contains these information. Rather than setting artificial boundaries for the categories of stain intensity, we retain a continuous description of the stain intensity. Only the information useful for predicting the H-Score is presented to a deep CNN to estimate the H-Score of the input image. This is in contrast to many work in the literature where the whole image is thrown to the CNN regardless if a region is useful or not for the purpose.

3.1 Stain Intensity Description

Although various DAB stain separation methods have been proposed [6], [25], few work studied the stain intensity description and grouping. Since there is no formal definitions for the boundaries between stain intensity groups (e.g, *strong*, *moderate*, *weak*), previous works used manually defined thresholds for pixel-wise classification to segment positive stains into each stain group [9].

In this work, we propose to directly use the luminance values of the image to describe the staining intensity instead of setting artificial intensity category boundaries. The original RGB image I is first transformed into three-channel stain component image ($I_{DAB-H} = [I_{DAB}, I_H, I_{Other}]$) using colour deconvolution [6]:

$$I_{DAB-H} = M^{-1} I_{OD}, \quad (2)$$

where M is the stain matrix composed of staining colours equal to

$$\begin{bmatrix} 0.268 & 0.570 & 0.776 \\ 0.650 & 0.704 & 0.286 \\ 0.0 & 0.0 & 0.0 \end{bmatrix} \quad (3)$$

for DAB-H stained images, and I_{OD} is Optical Density converted image calculated according Lambert-Beers law:

$$I_{OD} = -\log\left(\frac{I}{I_0}\right), \quad (4)$$

$I_0 = [255, 255, 255]$ is the spectral radiation intensity for a typical 8bit RGB camera [26]. Only the DAB channel image I_{DAB} from the three colour deconvolution output channels is used, which describes the DAB stain according the chroma difference.

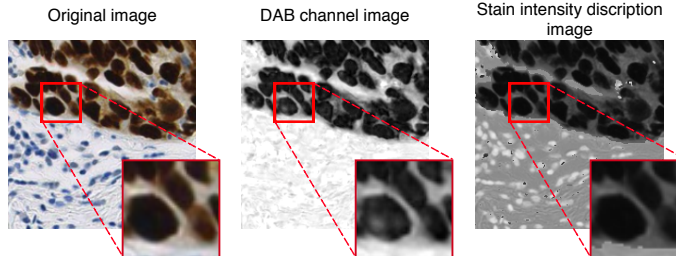


Fig. 4: A comparison of different images generated during the process of stain intensity description. The highlighted subimage contains strongly stained nuclei.

Most previous works set a single threshold on I_{DAB} to separate positively stained tissues. However, as shown in Fig.4, the deeply stained positive nuclei can have dark and light pixel values on the DAB channel image, since the strongly stained pixels will have significantly broader hue spectrum. The same DAB channel value can correspond to different stain intensities even different colours. In this paper, we use the Luminance Adaptive Multi-Thresholding (LAMT) method developed by the authors [27] to classify positively stained pixels. Specifically, the transformed pixel $I_{DAB}(m, n)$ is divided into K equal intervals according to the luminance:

$$I_{DAB}^k(m, n) = \{I_{DAB}^k(m, n) \in I_{DAB}) | \xi^k < I_l(m, n) \leq \zeta^k\} \quad (5)$$

where $k = 1, 2, \dots, K$; ξ^k and ζ^k are lower and upper bound respectively of the k th luminance interval. I_l is the luminance image of the original RGB image calculated according to Rec. 601 [28]:

$$I_l = 0.299 \times I_R + 0.587 \times I_G + 0.114 \times I_B. \quad (6)$$

The transformed pixels are thresholded with different values according to its luminance instead of a single threshold, the threshold t_k is assigned as follows:

$$t_k = \operatorname{argmax}_{c \in \mathcal{C}} P(c|I_{DAB}^k(m, n)) \quad (7)$$

where $\mathcal{C} = \{c_{DAB}, c_H\}$ is the stain label.

Once we have separated the positive stain from the negative stain, we need to find a way to describe the stain intensity. As we have already seen in Fig.4, the pixel values of I_{DAB} can not describe the biomarker stain intensity. We propose to use a scheme described in Eq.8 to assign stain intensity values to pixels:

$$I_{la}(m, n) = \begin{cases} I_l(m, n) & \text{if } I_{DAB}(m, n) \text{ is positive} \\ 255 + 255 - I_l(m, n) & \text{if } I_{DAB}(m, n) \text{ is negative} \end{cases} \quad (8)$$

where $I_{la}(m, n)$ is the stain intensity description image.

The idea is that for the positive stain pixels, $I_{la}(m, n)$ is the same as the luminance component of the original image in order to preserve the morphology of the positive nuclei; for the negative stain pixels, $I_{la}(m, n)$ will have a higher value for strongly stained pixels (darker blue colour) and a lower value for weakly stained pixels (lighter blue colour). In order to separate the positive and negative pixel values clearly, we add an offset of 255 to the negatively stained pixels (most negative stain pixels will have a high $I_l(m, n)$ and positive stain pixels will have a low $I_l(m, n)$, the value of positive and negative pixels will be clearly separated in $I_{la}(m, n)$). Therefore, the larger $I_{la}(m, n)$ is, the weaker the stain is; the smaller $I_{la}(m, n)$ is, the stronger is the stain. When $I_{la}(m, n)$ is below or equal to 255, it is a positive stain pixel. In this way, we have obtained an image which gives a continuous description of the stain intensity of the image. Instead of setting artificial boundaries to separate the different degrees of stain intensity, we now have a continuous description of the stain intensity (see Fig.5). Note that the pixel values of final image are normalized to the range from 0 to 1.

3.2 Nuclei and Tumour Maps

As discussed above, the important information pathologists use to come up with the H-Score is the number of nuclei and the number of tumour nuclei in the TMA image. We therefore need to extract these two pieces of information and we use two separate FCNs, one for segmenting the foreground region which contains all nucleus and the other for segmenting the region of tumour nucleus only.

Recent proposed fully convolutional network can take an input image of arbitrary size and produce a correspondingly-same-sized output by an encoder-decoder architecture [15], [29]. We add skip connections so that the high resolution features from the contracting path are combined with the output from the upsampling path, which allows the network to learn the high resolution contextual information. Specifically, skip connections are added between the last convolutional layer of each block in the encoder and the first layer of the corresponding block in the decoder. The loss function is designed according to the Dice coefficient as:

$$L_{mask} = -\frac{2 \sum_{m,n} \omega \tau}{\sum_{m,n} \omega + \sum_{m,n} \tau}, \quad (9)$$

where ω is the predicted pixel and τ is the ground truth.

To segment the tumour regions, we use our own manually pixel-wise labelled tumour TMA images to train the FCN; while transfer learning strategy is utilized for general nuclei detection, and the training data is obtained from three different datasets. Detailed datasets information well be presented in Section 4.1. Training on a mixed image set could help to reduce overfitting on limited medical dataset and further boost the performance and robustness [30].

3.3 The H-Score Prediction Framework

The detail of the first two stages have been described in Section 3.1 and 3.2. As illustrated in Fig.3, an input TMA image $I(m, n)$ is processed by the tumour detection network which will output a binary image mask, $T(m, n)$, marking all the tumour nuclei, where $T(m, n) = 1$ if $I(m, n)$ is a part of a tumour nuclei and $T(m, n) = 0$ otherwise; by the general nuclei detection network which will output another binary image mask, $G(m, n)$, marking all tumour and non-tumour nuclei, where $G(m, n) = 1$ if $I(m, n)$ is a part of a nuclei and $G(m, n) = 0$ otherwise; and by the colour deconvolution and stain intensity labelling operation of Equation (8) to produce the stain intensity description image $I_{la}(m, n)$.

In the third stage, we firstly construct SINI and SITI by multiplying the nuclei mask image $G(m, n)$ and tumour mask image $T(m, n)$ with the stain intensity description image $I_{la}(m, n)$, i.e. $SINI = I_{la}(m, n) \times G(m, n)$, and $SITI = I_{la}(m, n) \times T(m, n)$. Hence, all background pixels

are zero, while only region of interests (ROI) are retained in SINI and SITI. All necessary information is preserved for histochemical assessment. Removing the background and only retaining ROI will enable the RAM-CNN convolutional layers to focus on foreground objects [31] which will significantly reduce computational cost and improve performance.

layer name	output size	input size/ patch size, stride	
Input		$512 \times 512 \times 1$	$512 \times 512 \times 1$
Conv1	$512 \times 512 \times 8$	$7 \times 7 \times 8$	$7 \times 7 \times 8$
MaxPool	$128 \times 128 \times 8$	4×4 , stride 4	4×4 , stride 4
Conv2	$128 \times 128 \times 16$	$5 \times 5 \times 16$	$5 \times 5 \times 16$
MaxPool	$64 \times 64 \times 16$	3×3 , stride 2	3×3 , stride 2
Concat	$64 \times 64 \times 32$		
Conv3	$64 \times 64 \times 64$		$3 \times 3 \times 64$
MaxPool	$32 \times 32 \times 64$		3×3 , stride 2
Conv4	$32 \times 32 \times 64$		$3 \times 3 \times 64$
MaxPool	$16 \times 16 \times 64$		3×3 , stride 2
FC1	2048-d		2048
Dropout			0.3
FC2	1024-d		1024
Dropout			0.3
Output	1-d		1

TABLE 1: The architecture of Region Attention Multi-channel Convolutional Neural Network (RAM-CNN). The pipeline consists of convolutional layer (Conv), maxpooling layer (MaxPool), concatenation (Concat), and fully connected layer (FC).

The proposed RAM-CNN is a deep regression model with dual input channels. The architecture of RAM-CNN is shown in Table 1. Two inputs correspond to SINI and SITI respectively, and the input size is 512×512 . The parameters of the two individual branches are updated independently for extracting cell and tumour features respectively, without interfering with each other. The two pipelines are concatenated into one after the second convolutional-pooling block. Since the NPI+ dataset is small and the network requires large input image size, using very deep network such as ResNet [32] would lead to overfitting and huge computation cost. Rectified linear unit (ReLU) activation function are utilized for the convolutional layers, and linear activation function is applied for H-Score prediction. The loss function for H-Score prediction is defined as:

$$L_{score} = \frac{1}{N} \sum_{i=1}^N \|F_{RAM}(SINI_i, SITI_i) - l_i\|_2, \quad (10)$$

where $F_{RAM}(SINI_i, SITI_i)$ is the estimated score generated by RAM-CNN. l_i is the ground truth H-Score.

4 EXPERIMENTS AND RESULTS

4.1 Datasets

The H-Score dataset used in our experiment contains 105 TMA images of breast adenocarcinomas from the NPI+

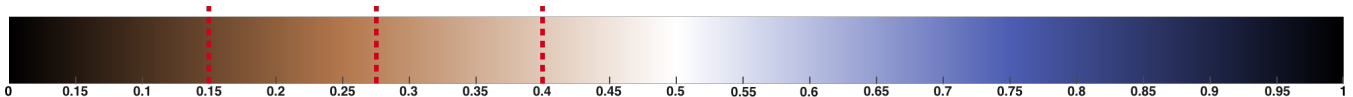


Fig. 5: An illustration of the value of l_{la} and its corresponding stain intensity. The red dot lines are the thresholds of stain intensity groups [9].

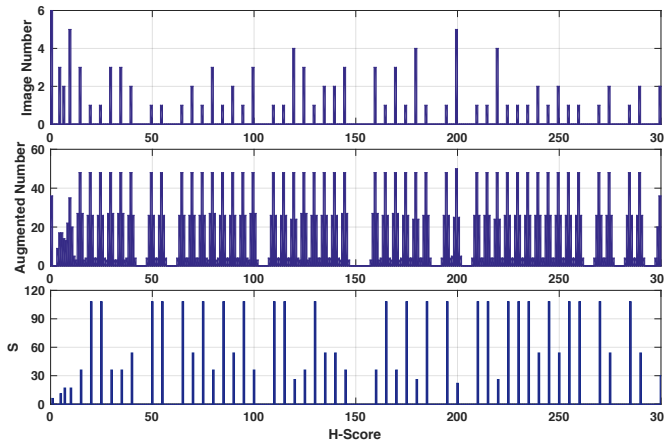


Fig. 6: The top graph is the original dataset label histogram; The Middle is the augmented label histogram; The bottom is the augmented label number (S) for each image according to its corresponding H-Score.

set [1]. Each image contains one whole TMA core. The tissues are cropped from a sample of one patient which are stained with three different nuclei activity biomarkers: ER, p53, and PgR. The original images are captured at a high resolution of $40\times$ optical magnification, and then resized to $1024\times 1024\times 3$ pixels. The dataset is manually marked by two experienced pathologists with H-Score based on common practice. For each TMA core, the pathologists give the percentage of nuclei of different stain intensity levels, and then calculate the H-Score using Eq.1. The final label (H-Score) is determined by averaging two pathologists' scores. The dataset is available from the authors on request.

To train the general nuclei detection network, we constructed a mixed dataset consist of 3997 images by randomly cropping 224×224 image patches without overlapping from immunofluorescence (IIF) stained HEp-2 cell dataset (1932 images) [33], Warwick hematoxylin and eosin (H&E) stained colon cancer dataset (1840 images) [34], and our own DAB-H stained NPI+ images (115 images). Since these three image sets are stained with different types of biomarker, we transform the colour image into grayscale for training. As HEp-2 cell images are IIF stained, the gray value should be inversed. We labelled 33 DAB-H stained TMA core images (outside of H-Score dataset), and we also random cropped image patches for training the tumour detection network.

4.2 Data and Label Augmentation

As in typical medical imaging applications, the dataset sizes are relatively small. In developing deep learning based solutions, it is a common practice to augment the training dataset for training. The training images for general nuclei detection network and tumour detection network are augmented by randomly cropping sub-images as input samples. For the H-Score dataset, rotation with random angles and randomly shifting the image horizontally and vertically within 5% of image height and width are performed to augment the training set.

As shown in the top row of Fig.6, the distribution of the label (H-Score) in the original dataset is unbalanced, some labels (H-Scores) have far more samples than others.

Furthermore, one of the biggest problems is that because we have only limited number of samples, the H-Score values are discrete and discontinuous. There are many gaps between two H-Scores that has no data. Also, the values of the TMA image score given by the pathologists have a quantitative step-size of 5. Therefore, if an image has a score of 125, it means it has a value of around 125, the values in the vicinity of 125, i.e., 126 or 124 should also be suitable for labelling that image. In order to solve the ambiguity issue, we introduce Distributed Label Augmentation (DLA) which was inspired by the work of [35], [36].

In the traditional regression method, a given dataset $\{(I_1, l_1), (I_2, l_2), \dots, (I_D, l_D)\}$ pairs the instance I_d for $1 \leq d \leq D$ with one single l_d from the finite class label space $\mathcal{L} = \{l^0, l^1, \dots, l^C\}$, where C is the label size (e.g., $C = 301$ for H-Score). In this paper, the label is augmented so that one instance is associated with a number of labels. Formally, the dataset can be described as $\{(I_1, Y_1), (I_2, Y_2), \dots, (I_D, Y_D)\}$, and $Y_d \subseteq \mathcal{Y}$ is a set of labels $\{y_d^{(1)}, y_d^{(2)}, \dots, y_d^{(S)}\}$, where S is the augmented label number for I_d . $y_d^{(s)}$ is sampled repeatedly from \mathcal{L} based on a probability density function of following Gaussian distribution:

$$p(y_d^{(s)} = l^c) = \frac{1}{\sigma\sqrt{2\pi}} \exp\left(-\frac{(l^c - \mu)^2}{2\sigma^2}\right) \quad (11)$$

where μ is the mean which equal to l_d and σ is standard deviation. Thus, $\sum_{s=1}^S p(y_d^{(s)}) = 1$ for each original TMA image. Consequently, for an image x_i from the augmented training set, its ground truth labels are assigned by repeatedly sampling from \mathcal{L} according to Eq.11. The augmented label histogram is shown at the bottom row of Fig.6.

4.3 Implementation Details

We employ U-Net [15] architecture for both the tumour nuclei detection and general nuclei detection models in a straightforward fashion. We add dropout layers after the first convolutional layer in each encoding and decoding block with the rate of 0.1. The filter size of tumour detection net is half narrower than that of general cell detection net. The final cell and tumour region maps are predicted using sliding window.

A leave 5 out cross validation strategy is used for RAM-CNN model training, which means that in each round of testing, we randomly sample 5 TMAs as testing and the other 100 TMAs as training images. As explained previously, the training set is augmented via rotation and shift. Specifically, the data is firstly balanced with random horizontally and vertically shift within 10% of image edge length, and then augment the dataset to 5314 images. The images are firstly resized to 512×512 before fed into the RAM-CNN. We set $\sigma = 0.9$ to generate the H-Score distribution for ground truth label augmentation, to ensure the augmented labels are within the range of plus or minus 2 around the ground truth. The regression network is optimized by Adam [37] with a constant learning rate of 0.001.

4.4 Results and Discussions

4.4.1 intermediate results

Fig.7 shows some examples of the intermediate images in the automatic H-Score prediction pipeline. It is seen that

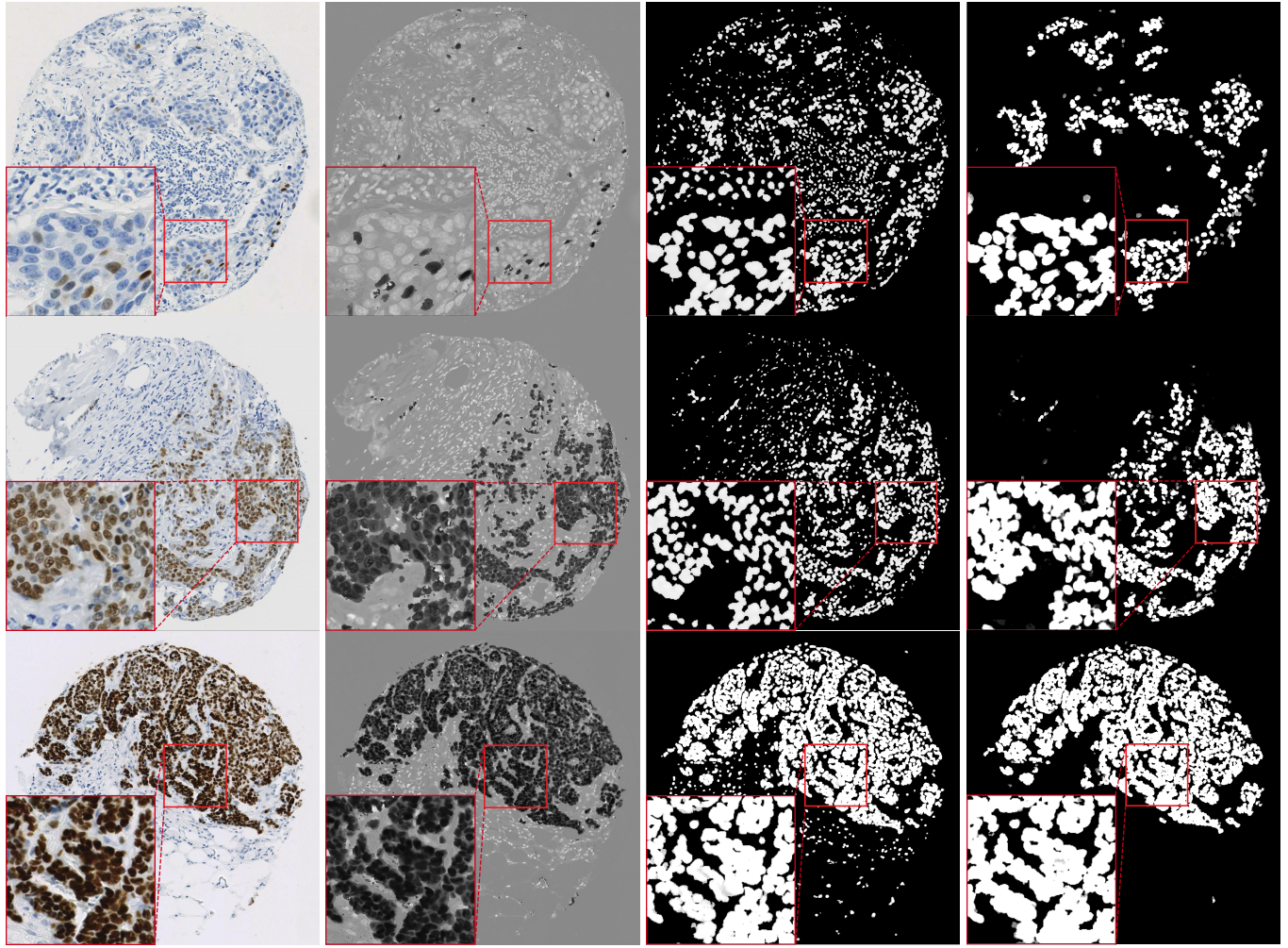


Fig. 7: Examples of intermediate images in the automatic H-Score prediction pipeline. From left to right: the original RGB image, luminance labelled stain intensity image, nuclei mask image, and tumour mask image respectively.

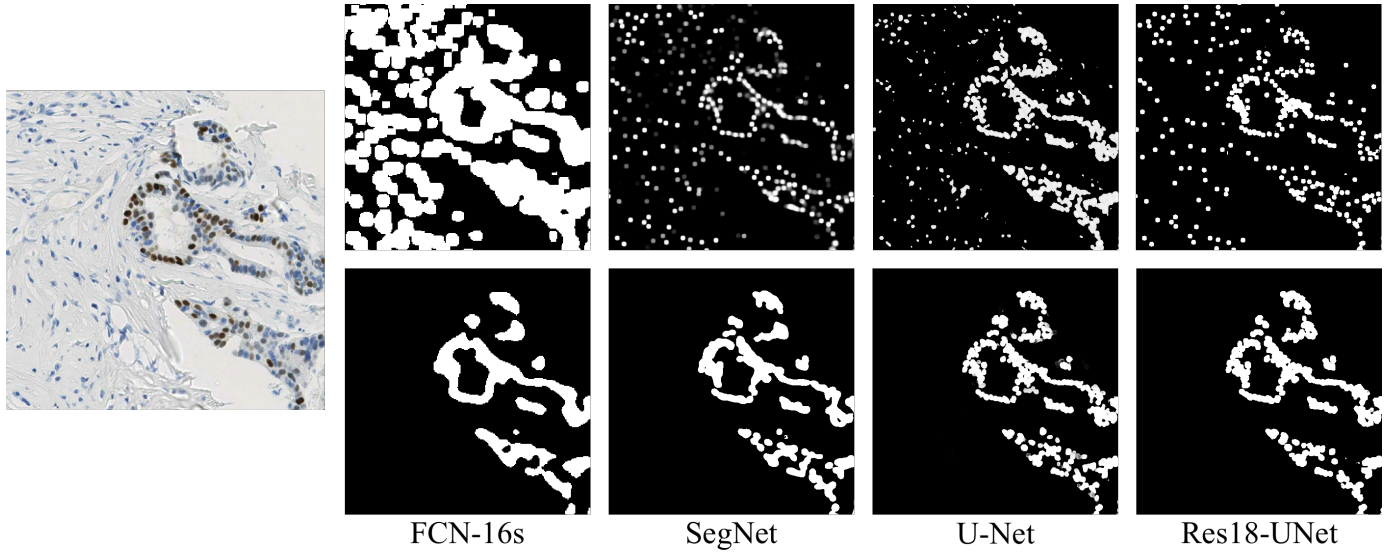


Fig. 8: Results of segmentation obtained with FCN-16s, SegNet, U-Net, and Res18-U-Net. The top row is the general nuclei segmentation results, while bottom row represents the tumour segmentation results.

the luminance labelled stain intensity image marks a sharp distinction between positive and negative stains. This shows

that our maximum a posteriori (MAP) classifier based Luminance Adaptive Multi-Thresholding (LAMT) method [27]

can reliably separate positive DAB stains for a variety of images. It also shows that our stain intensity labelling strategy can preserve the morphology of the nuclei, separate positive and negative stains while retaining a continuous description of the positive stain intensity.

We evaluated the segmentation performance in terms of pixel-wise distance metrics, e.g. Dice coefficient (DC) and segmentation accuracy (SA) [38]:

$$DC(PM, GTM) = \frac{|PM \cap GTM|}{|PM| + |GTM|} \quad (12)$$

$$SA = 1 - \frac{\text{Total no. of misclassified pixels}}{\text{Total no. of pixels in the image}} \quad (13)$$

where PM indicates a predicted mask, and GM means the ground truth mask.

Model	General Nuclei		Tumour	
	DC	SA	DC	SA
ARGraph	0.4535	0.5063	-	-
ImageJ IHC IAT	0.4732	0.5278	-	-
FCN-16s	0.5018	0.5788	0.6832	0.7142
SegNet	0.7961	0.8360	0.8460	0.8730
U-Net	0.8384	0.8816	0.8782	0.9219
Res18-UNet	0.8860	0.9716	0.8704	0.9799

TABLE 2: Quantitative comparison of different methods for general nuclei segmentation and tumour nuclei segmentation.

The U-Net is compared with widely used segmentation network of FCN-16s [39], SegNet [40], and Res18-UNet residual encoder network of ResNet18 [32]; two conventional unsupervised cell nuclei segmentation methods, ARGraph [13] and NIH ImageJ [41] IHC Image Analysis Toolbox plugin [14], which are unable to distinguish tumour nucleus from normal nucleus. Deep learning based models are superior to conventional methods. The U-Net achieves the highest Dice coefficient on tumour segmentation task while Res18-UNet provides the best performance on general nuclei segmentation (see Table.2). Example segmentation results in NPI+ dataset are shown in Fig.8. It can be seen that all four models can correctly segment the general nucleus and tumour regions. U-Net and Res18-UNet produced relatively more accurate segmentation results compared to FCN-16s and SegNet. The impact of segmentation accuracy on H-Score prediction is evaluated in Section 4.4.3.

More segmentation results generated by U-Net are illustrated in Fig.7. The nuclei mask images show that the deep convolutional network trained with mixed datasets using transfer learning can successfully detect the nuclei in our H-Score dataset. The tumour segmentation network is able to identify tumour region from normal tissues. It is worth noting that the ground truth masks for the two detection networks are different. All nucleus in Warwick colon cancer images are labelled with circular masks with a uniform size, while tumour region masks are pixel level labelled. Therefore, the final predicted maps generated by the two networks for the same nucleus are different. In addition, it is found that the mask dilation become evident with the increase of DAB stain intensity. One possible reason is that the strong homogeneous stain makes the nuclei texture and edge feature difficult to extract.

4.4.2 H-Score prediction results

We compared the proposed model, RAM-CNN, with two baseline single input pipeline CNNs: RGB-CNN and RA-CNN (i.e., region attention CNN), and two well-established models: AlexNet [42] and ResNet-18 [32]. The RGB-CNN takes the original RGB TMA image with the shape of $512 \times 512 \times 3$ as input, and output the H-Score prediction. To investigate the effect of multi-column architecture, we combine SINI and SITI as a two channel image of $512 \times 512 \times 2$ for the input of RA-CNN. The architectures of RGB-CNN and RA-CNN are the same as a single pipeline RAM-CNN (see Table.1). We also calculate the H-Score using Eq.1 based on the nuclei area percentage (NAP) and nuclei number percentage (NNP). Specifically, the luminance labelled stain intensity description image I_{la} is first calculated according to the description in Section 3.1. The pre-defined thresholds [9] are utilized for categorizing the pixels into different DAB-H stain intensity groups. For the NAP method, the predicted H-Score is calculated according to the percentages of area in different stain intensity groups. NNP employs the NIH ImageJ tool [41] with a multi-stage cell segmentation technique [14] for cell detection. The detected cells are classified into *unstained*, *weak*, *moderate*, and *strong* groups using the pre-defined thresholds [9] (see Fig.5) for H-Score calculation.

Model	MAE	SD	CC	P value
NAP	47.09	46.03	0.868	< 0.001
NNP	46.48	55.18	0.824	< 0.001
AlexNet	29.47	37.78	0.913	< 0.001
ResNet-18	40.03	52.54	0.835	< 0.001
RGB-CNN	32.01	44.46	0.873	< 0.001
RA-CNN	27.22	35.72	0.922	< 0.001
RAM-CNN	21.33	29.14	0.949	< 0.001
Human	20.63	30.55	0.954	< 0.001

TABLE 3: Performance comparison with different regression models. The last line (Human) are difference between the H-Scores given by the two pathologists.

In this paper, Mean Absolute Error (MAE), Standard Deviation (SD) and the correlation coefficient (CC) between the predicted H-Score and the average H-Score of the two pathologists are used as the evaluation metrics. As a reference, we also calculate the MAE, SD and CC between the H-Scores given by the two pathologists of all original diagnosis data.

As can be seen from Table.3, the NAP based prediction gives the highest MAE with large deviations in the cross validation, which is followed by NNP. Our RAM-CNN framework achieves the lowest prediction error (21.33); a traditional CNN setting with the proposed SINI and SITI as input gives the second lowest prediction error (27.22). This verifies the effectiveness of our proposed approach to filtering out irrelevant pixels and only retain H-Score relevant information in SINI and SITI. All deep learning based methods outperform NAP and NNP by a large margin, except ResNet-18 which has an MAE of 40.03. One reason is that the very deep model easily leads to overfitting. AlexNet with large convolutional kernels achieves better result than RGB-CNN and ResNet-18. To investigate the statistical significance of automatically predicted H-Scores,

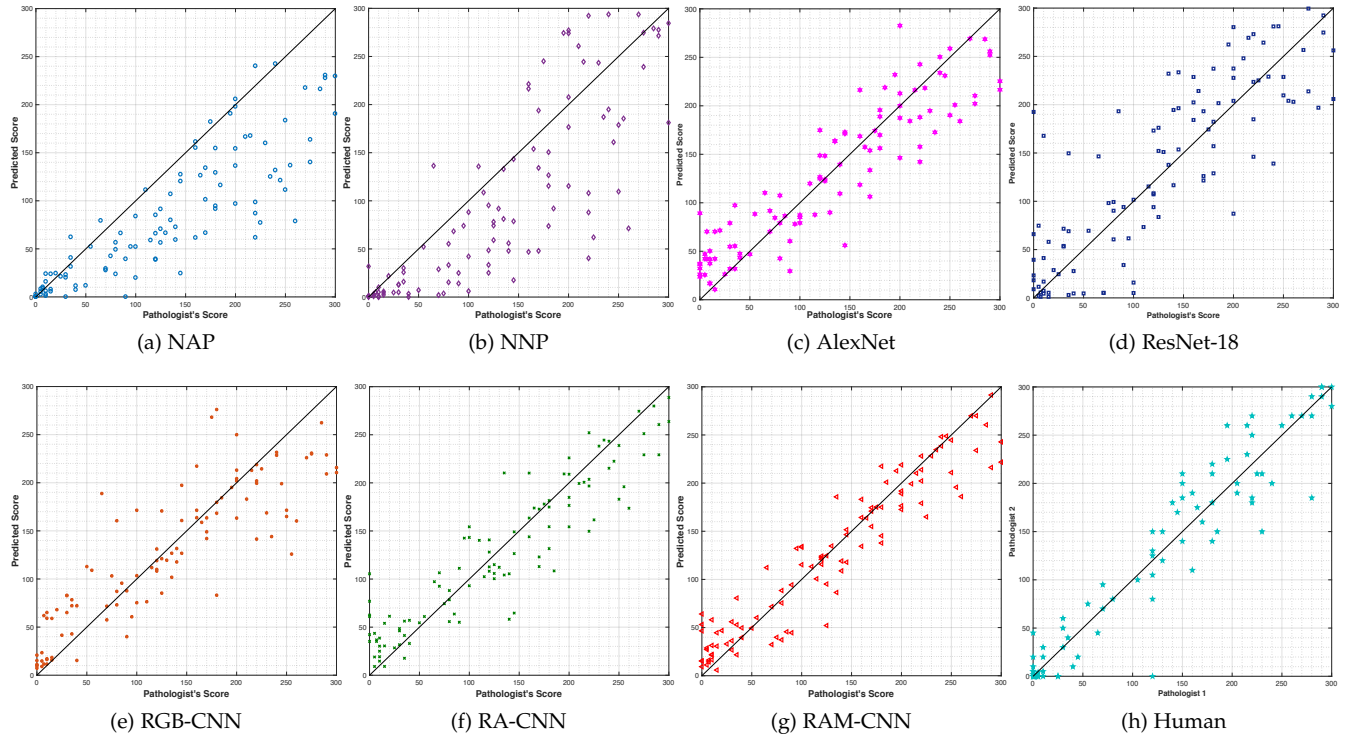


Fig. 9: (a-g) are the scatter plots of the predicted scores of different models vs the pathologists' manual scores; (h) is the scatter plot of the scores of assessed by two different pathologists.

the correlation of the predicted and those of the pathologists scores and its P value are also calculated. The correlation between pathologists scores and those predicted by RAM-CNN is 0.949 with a P value of < 0.001 , which means the correlation is considered significant and there is strong evidence against the null hypothesis that there is no relationship between pathologists scores and predicted scores [43].

It is interesting to observe that the difference between our RAM-CNN predicted H-Scores and the average of the two pathologists H-Scores ($MAE = 21.33$, $SD = 29.14$, $CC = 0.949$) are on par with the difference between the two pathologists ($MAE = 20.63$, $SD = 30.55$, $CC = 0.954$). While the MAE between the RAM-CNN and humans is slightly higher than that between humans, the SD between humans is higher than that between RAM-CNN and humans. The CC between humans and machine and that between humans are the same.

Fig.9 illustrates the scatter plots between the model predicted scores and the pathologists' scores. Most of the predicted scores of NAP are lower than the ground truth. At the lower end, NNP predicted scores are lower than the ground truth while at the higher end the predicted scores are higher than the ground truth. These two methods are affected by several low-level processing components including the pre-defined stain intensity thresholds and the nuclei segmentation accuracy. Our proposed framework gives more accurate prediction results compared to traditional baseline CNN, further demonstrating that imitating the pathologists' H-Scoring process by only keeping useful information is an effective approach.

4.4.3 segmentation accuracy and label augmentation evaluation

The objective of this section is to evaluate the impact of segmentation accuracy on H-Score prediction and the usefulness of label augmentation.

Model	Segmentation Accuracy (DC)		H-Score Prediction	
	General Nuclei	Tumour	MAE	SD
FCN	0.5018	0.6832	28.41	35.79
SegNet	0.7961	0.8460	25.74	33.78
U-Net	0.8384	0.8782	21.33	29.14
Res18-UNet	0.8860	0.8704	22.64	31.59

TABLE 4: Performance comparison of H-Score prediction with different general nuclei and tumour nuclei segmentation models.

Table.4 compares the H-Score prediction results of RAM-CNN with different general nuclei and tumour nuclei segmentation models. It can be observed that the performance of RAM-CNN is improved with the segmentation accuracy. However, Res18-UNet with the best general nuclei segmentation performance has a slightly higher MAE than that using U-Net. One possible reason is that the training set of general nuclei segmentation is consist of three different types of histopathology images with different label masks, and the well-trained model may less compatible with NPI+ dataset.

To investigate the impact of label augmentation, we compare the MAE of different H-Score prediction model with or without using label augmentation. Fig.10 clearly shows that label augmentation can promote the prediction performance of our proposed models.

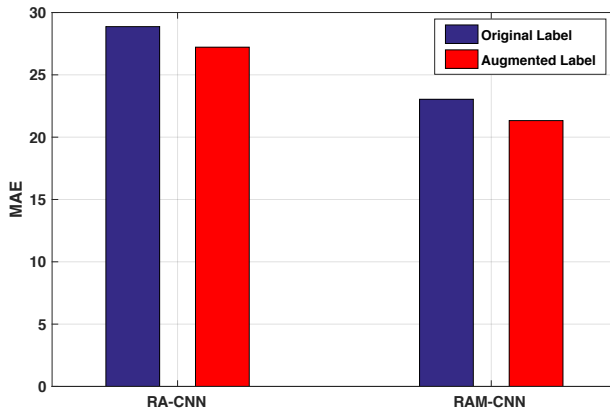


Fig. 10: Performance comparison with or without using label augmentation.

4.4.4 Discussions

In this paper, we introduced an end-to-end system to predicted H-Score. To gain an insight into the scoring discrepancy between the proposed algorithm and the pathologists, we firstly compare the H-Score prediction results for different biomarkers as shown in Table.5. The proposed framework gives the best accuracy in all three biomarker images. The performances are slightly different for different biomarkers. This is to be expected because different markers will stain the tissues differently. Although the difference is not large, whether it will be useful to train a separate network for different biomarkers is something worth investigating in the future.

Biomarker	ER	P53	PgR
No. of TMA	32	33	40
NAP	42.02	50.68	48.17
NNP	43.53	46.72	48.92
AlexNet	30.65	28.16	29.62
ResNet-18	34.91	39.35	44.67
RGB-CNN	24.90	31.57	38.19
RA-CNN	25.43	23.39	31.82
RAM-CNN	21.01	16.66	25.44

TABLE 5: Comparing MAE of different methods on three different biomarkers.

To see how the algorithms perform differently across the dataset, we divide the TMA images into 6 groups according to their pathologists' scores. For each group, we count the number of TMAs with absolute error (AE) smaller than 10, between 10 and 30, and larger than 30 respectively. The results of different methods are shown in Fig.11. It is seen that in the low H-Score group of 0-49, traditional methods of NAP and NNP give more accurate predicted scores than CNN based methods. It is found that most low score TMAs are unstained or weakly stained. The accurate predictions from NAP and NNP indicate that the predefined threshold for separating *unstained* and *weak* (see Fig. 5) is compatible with pathologists' criteria. The deep learning based methods do not set stain intensity thresholds explicitly and their performances across the six groups are relatively even.

The accuracies of NAP and NNP decrease rapidly with the increase of the H-Score. The stain intensity and image complexity increase with the H-Score which directly affect

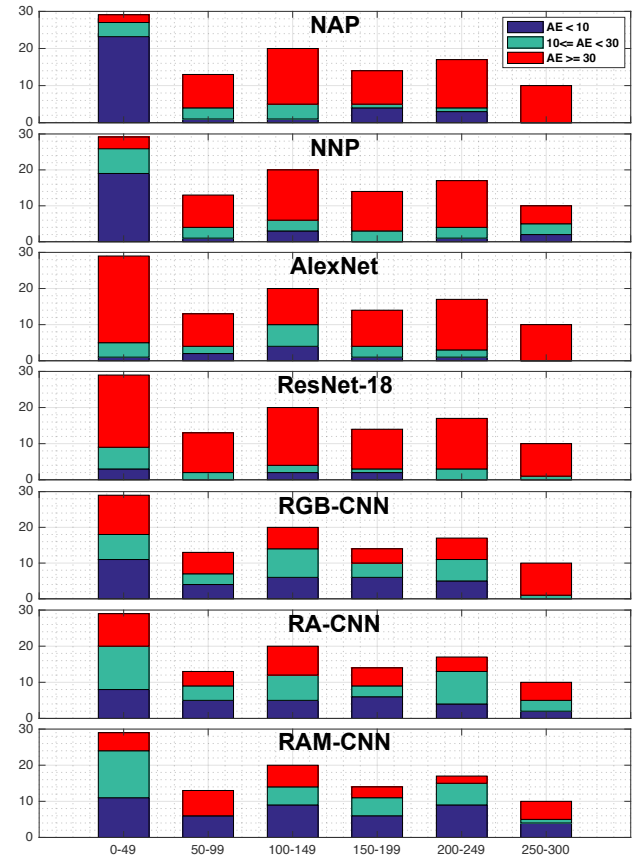


Fig. 11: Comparison of performances of different methods in different H-Score groups.

the performance of traditional methods. The result also indicates that the pre-defined stain intensity thresholds for *moderate* and *strong* classes (see Fig. 5) are less compatible with the pathologists' criteria. Furthermore, the large coefficients of *moderate* and *strong* stain (see Eq.1) would magnify the errors of area and nuclei segmentation in NAP and NNP respectively. The deep learning based methods give worse results on the groups with fewer images (i.e., group 50-99 and 250-300), which indicates the importance of a large training data size. It is also found that AlexNet produces more prediction results with AE larger than 30 than RGB-CNN, despite the overall MAE is lower.

We further analyse the TMAs individually to investigate the effect of image quality on the proposed algorithm. We found that for those TMAs where the tissues are clearly stained, and the cellular structure is clear without severe overlap, our algorithm can give very accurate prediction (see Fig.13). On the other hand, poor image quality causes errors. In the images that are most easily mis-scored by our algorithms, we found three significant characteristics as shown in Fig.12.

The TMA core in Fig.12(a) contains large out-of-focus regions, which happens more commonly on strongly stained tissues. The blur regions directly affect the performance of nuclei segmentation, as well as the nuclei and tumour detection accuracy. They also hinder the final regression network from extracting topological and morphological information.

Tissue folds (see Fig.12(b)) occurs when a thin tissue slice

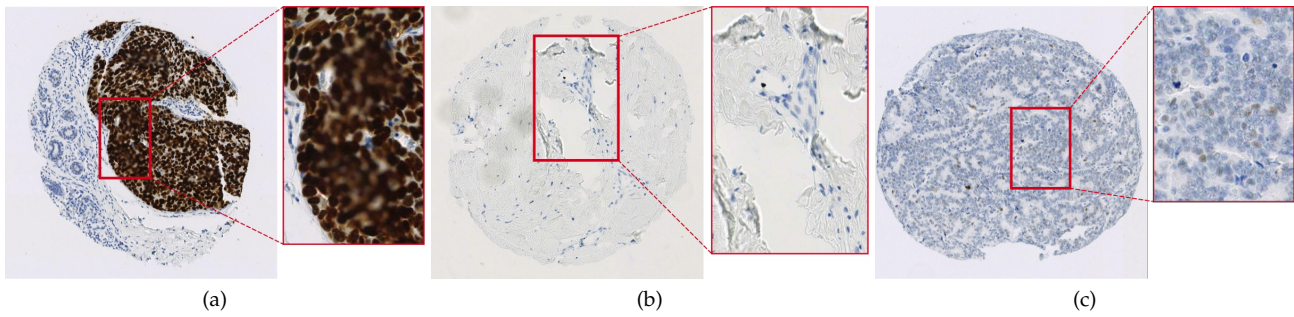


Fig. 12: Examples of sources of big scoring discrepancy between algorithm and pathologist. (a) out of focus; (b) tissue folds; (c) heterogeneity and overlapping.

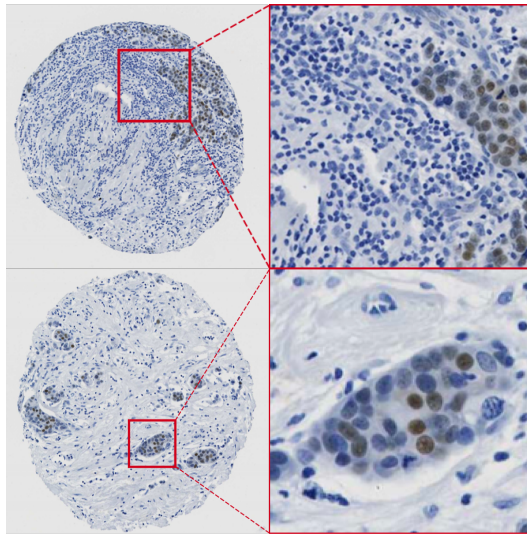


Fig. 13: Examples of accurately scored TMAs by proposed algorithm. The absolute errors generated by RAM-CNN of both two TMAs are smaller than 2.

folds on itself, and it can happen easily during slide preparation especially in TMA slides. Tissue-fold would cause out-of-focus during slide scanning. Furthermore, a tissue fold in a lightly stained image can be similar in appearance to a tumour region in a darkly stained image [44]. Hence, the segmentation accuracy of colour deconvolution would be greatly affected in tissue-fold regions.

Heterogeneity and overlapping as shown in Fig.12(c) also affect the automatic scoring performance. The stain heterogeneity gives rise to a large discrepancy of stain intensity in a single nucleus, and nuclei overlapping adds to the difficulty.

These three difficulties directly affect the predicted results of the proposed method, and we found that most large mis-scored TMAs contain one or more of these characteristics. We found that there were 9 low image quality TMAs in our dataset and if we exclude these 9 lowest-quality TMA images, the average MAE of our RAM-CNN is 18.79. Therefore, future works need to overcome these issues in order to achieve a high prediction performance. To solve the problem of out-of-focus, heterogeneity and overlapping, adding corresponding images in the training

set to promote robustness is one potential quality assurance methods. Image pre-processing using variational models with certain prior knowledges are also recommended [45], [46]. In addition, the deep learning based scoring system can be developed to add nuclei number estimation function for accurate assessment. It is also necessary to add the function of automated detection and elimination of tissue-fold regions before H-Score assessment.

5 CONCLUDING REMARKS

In this paper, we have developed a deep learning framework for automatic end-to-end H-Score assessment for breast cancer TMAs. Experimental results show that automatic assessment for TMA H-Score is feasible. The H-Scores predicted by our model have a high correlation with H-Scores given by experienced pathologists. We show that the discrepancies between our deep learning model and the pathologists are on par with those between the pathologists. We have identified image out of focus, tissue fold and overlapping nuclei as the three major sources of error. We also found that the major discrepancies between pathologists and machine predictions occurred in images that will have a high H-Score value. These findings have suggested future research directions for improving accuracy.

REFERENCES

- [1] E. Rakha, D. Soria, A. R. Green, C. Lemetre, D. G. Powe, C. C. Nolan, J. M. Garibaldi, G. Ball, and I. O. Ellis, "Nottingham prognostic index plus (npi+): a modern clinical decision making tool in breast cancer," *British journal of cancer*, vol. 110, no. 7, pp. 1688–1697, 2014.
- [2] T. O. Nielsen, J. S. Parker, S. Leung, D. Voduc, M. Ebbert, T. Vickery, S. R. Davies, J. Snider, I. J. Stjleman, J. Reed *et al.*, "A comparison of pam50 intrinsic subtyping with immunohistochemistry and clinical prognostic factors in tamoxifen-treated estrogen receptor-positive breast cancer," *Clinical cancer research*, pp. 1078–0432, 2010.
- [3] A. Green, D. Powe, E. Rakha, D. Soria, C. Lemetre, C. Nolan, F. Barros, R. Macmillan, J. Garibaldi, G. Ball *et al.*, "Identification of key clinical phenotypes of breast cancer using a reduced panel of protein biomarkers," *British journal of cancer*, vol. 109, no. 7, p. 1886, 2013.
- [4] H. Goulding, S. Pinder, P. Cannon, D. Pearson, R. Nicholson, D. Snead, J. Bell, C. Elston, J. Robertson, R. Blamey *et al.*, "A new immunohistochemical antibody for the assessment of estrogen receptor status on routine formalin-fixed tissue samples," *Human pathology*, vol. 26, no. 3, pp. 291–294, 1995.

- [5] A. C. Ruifrok, "Quantification of immunohistochemical staining by color translation and automated thresholding," *Analytical and quantitative cytology and histology/the International Academy of Cytology [and] American Society of Cytology*, vol. 19, no. 2, pp. 107–113, 1997.
- [6] A. C. Ruifrok, D. A. Johnston *et al.*, "Quantification of histochemical staining by color deconvolution," *Analytical and quantitative cytology and histology*, vol. 23, no. 4, pp. 291–299, 2001.
- [7] H. Irshad, A. Veillard, L. Roux, and D. Racoceanu, "Methods for nuclei detection, segmentation, and classification in digital histopathology: a review current status and future potential," *IEEE reviews in biomedical engineering*, vol. 7, pp. 97–114, 2014.
- [8] H. Masmoudi, S. M. Hewitt, N. Petrick, K. J. Myers, and M. A. Gavrielides, "Automated quantitative assessment of her-2/neu immunohistochemical expression in breast cancer," *IEEE transactions on medical imaging*, vol. 28, no. 6, pp. 916–925, 2009.
- [9] N. Trahern, Y. W. Tsang, I. A. Cree, D. Snead, D. Epstein, and N. Rajpoot, "Simultaneous automatic scoring and co-registration of hormone receptors in tumor areas in whole slide images of breast cancer tissue slides," *Cytometry Part A*, 2016.
- [10] N.-A. Pham, A. Morrison, J. Schwock, S. Aviel-Ronen, V. Iakovlev, M.-S. Tsao, J. Ho, and D. W. Hedley, "Quantitative image analysis of immunohistochemical stains using a cmyk color model," *Diagnostic pathology*, vol. 2, no. 1, p. 8, 2007.
- [11] D. Anoraganingrum, "Cell segmentation with median filter and mathematical morphology operation," in *Image Analysis and Processing, 1999. Proceedings. International Conference on*. IEEE, 1999, pp. 1043–1046.
- [12] K. Jiang, Q.-M. Liao, S.-Y. Dai *et al.*, "A novel white blood cell segmentation scheme using scale-space filtering and watershed clustering," in *Proceedings of the 2003 International Conference on Machine Learning and Cybernetics*. IEEE, 2003, pp. 2820–2825.
- [13] S. Arslan, T. Ersahin, R. Cetin-Atalay, and C. Gunduz-Demir, "Attributed relational graphs for cell nucleus segmentation in fluorescence microscopy images," *IEEE transactions on medical imaging*, vol. 32, no. 6, pp. 1121–1131, 2013.
- [14] J. Shu, H. Fu, G. Qiu, P. Kaye, and M. Ilyas, "Segmenting overlapping cell nuclei in digital histopathology images," in *Engineering in Medicine and Biology Society (EMBC), 2013 35th Annual International Conference of the IEEE*. IEEE, 2013, pp. 5445–5448.
- [15] O. Ronneberger, P. Fischer, and T. Brox, "U-net: Convolutional networks for biomedical image segmentation," in *International Conference on Medical Image Computing and Computer-Assisted Intervention*. Springer, 2015, pp. 234–241.
- [16] Y. Han and J. C. Ye, "Framing u-net via deep convolutional framelets: Application to sparse-view ct," *IEEE transactions on medical imaging*, vol. 37, no. 6, pp. 1418–1429, 2018.
- [17] A. P. Harrison, Z. Xu, K. George, L. Lu, R. M. Summers, and D. J. Mollura, "Progressive and multi-path holistically nested neural networks for pathological lung segmentation from ct images," in *International Conference on Medical Image Computing and Computer-Assisted Intervention*. Springer, 2017, pp. 621–629.
- [18] Y. Li, L. Shen, and S. Yu, "Hep-2 specimen image segmentation and classification using very deep fully convolutional network," *IEEE Transactions on Medical Imaging*, 2017.
- [19] S. Albarqouni, C. Baur, F. Achilles, V. Belagiannis, S. Demirci, and N. Navab, "Aggnets: deep learning from crowds for mitosis detection in breast cancer histology images," *IEEE transactions on medical imaging*, vol. 35, no. 5, pp. 1313–1321, 2016.
- [20] Y. Liu, K. Gadepalli, M. Norouzi, G. E. Dahl, T. Kohlberger, A. Boyko, S. Venugopalan, A. Timofeev, P. Q. Nelson, G. S. Corrado *et al.*, "Detecting cancer metastases on gigapixel pathology images," *arXiv preprint arXiv:1703.02442*, 2017.
- [21] D. Wang, A. Khosla, R. Gargoya, H. Irshad, and A. H. Beck, "Deep learning for identifying metastatic breast cancer," *arXiv preprint arXiv:1606.05718*, 2016.
- [22] M. Shah, C. Rubadue, D. Suster, and D. Wang, "Deep learning assessment of tumor proliferation in breast cancer histological images," *arXiv preprint arXiv:1610.03467*, 2016.
- [23] B. H. Hall, M. Ianosi-Irimie, P. Javidian, W. Chen, S. Ganeshan, and D. J. Foran, "Computer-assisted assessment of the human epidermal growth factor receptor 2 immunohistochemical assay in imaged histologic sections using a membrane isolation algorithm and quantitative analysis of positive controls," *BMC Medical Imaging*, vol. 8, no. 1, p. 11, 2008.
- [24] Z. Xinliang, Y. Jiawen, Z. Feiyun, and H. Junzhou, "Wsisa: Making survival prediction from whole slide pathology images," in *CVPR*, 2017.
- [25] E. M. Brey, Z. Lalani, C. Johnston, M. Wong, L. V. McIntire, P. J. Duke, and C. W. Patrick Jr, "Automated selection of dab-labeled tissue for immunohistochemical quantification," *Journal of Histochemistry & Cytochemistry*, vol. 51, no. 5, pp. 575–584, 2003.
- [26] P. Haub and T. Meckel, "A model based survey of colour deconvolution in diagnostic brightfield microscopy: Error estimation and spectral consideration," *Scientific reports*, vol. 5, 2015.
- [27] J. Liu, G. Qiu, and L. Shen, "Luminance adaptive biomarker detection in digital pathology images," *Procedia Computer Science*, vol. 90, pp. 113–118, 2016.
- [28] I. REC, "Bt. 601-5: Studio encoding parameters of digital television for standard 4: 3 and wide-screen 16: 9 aspect ratios," 1995.
- [29] W. Xie, J. A. Noble, and A. Zisserman, "Microscopy cell counting and detection with fully convolutional regression networks," *Computer methods in biomechanics and biomedical engineering: Imaging & Visualization*, vol. 6, no. 3, pp. 283–292, 2018.
- [30] H. Chen, X. Qi, L. Yu, and P.-A. Heng, "Dcan: Deep contour-aware networks for accurate gland segmentation," in *Proceedings of the IEEE conference on Computer Vision and Pattern Recognition*, 2016, pp. 2487–2496.
- [31] X. Li, Z. Liu, P. Luo, C. C. Loy, and X. Tang, "Not all pixels are equal: Difficulty-aware semantic segmentation via deep layer cascade," 2017.
- [32] K. He, X. Zhang, S. Ren, and J. Sun, "Deep residual learning for image recognition," in *Proceedings of the IEEE conference on computer vision and pattern recognition*, 2016, pp. 770–778.
- [33] P. Hobson, B. C. Lovell, G. Percannella, A. Saggese, M. Vento, and A. Willem, "Hep-2 staining pattern recognition at cell and specimen levels: datasets, algorithms and results," *Pattern Recognition Letters*, vol. 82, pp. 12–22, 2016.
- [34] K. Sirinukunwattana, S. E. A. Raza, Y.-W. Tsang, D. R. Snead, I. A. Cree, and N. M. Rajpoot, "Locality sensitive deep learning for detection and classification of nuclei in routine colon cancer histology images," *IEEE transactions on medical imaging*, vol. 35, no. 5, pp. 1196–1206, 2016.
- [35] B.-B. Gao, C. Xing, C.-W. Xie, J. Wu, and X. Geng, "Deep label distribution learning with label ambiguity," *IEEE Transactions on Image Processing*, 2017.
- [36] Z.-H. Zhou, M.-L. Zhang, S.-J. Huang, and Y.-F. Li, "Multi-instance multi-label learning," *Artificial Intelligence*, vol. 176, no. 1, pp. 2291–2320, 2012.
- [37] D. Kingma and J. Ba, "Adam: A method for stochastic optimization," *arXiv preprint arXiv:1412.6980*, 2014.
- [38] M. Saha and C. Chakraborty, "Her2net: A deep framework for semantic segmentation and classification of cell membranes and nuclei in breast cancer evaluation," *IEEE Transactions on Image Processing*, vol. 27, no. 5, pp. 2189–2200, 2018.
- [39] J. Long, E. Shelhamer, and T. Darrell, "Fully convolutional networks for semantic segmentation," in *Proceedings of the IEEE conference on computer vision and pattern recognition*, 2015, pp. 3431–3440.
- [40] V. Badrinarayanan, A. Kendall, and R. Cipolla, "Segnet: A deep convolutional encoder-decoder architecture for image segmentation," *IEEE transactions on pattern analysis and machine intelligence*, vol. 39, no. 12, pp. 2481–2495, 2017.
- [41] C. A. Schneider, W. S. Rasband, and K. W. Eliceiri, "Nih image to imagej: 25 years of image analysis," *Nature methods*, vol. 9, no. 7, pp. 671–675, 2012.
- [42] A. Krizhevsky, I. Sutskever, and G. E. Hinton, "Imagenet classification with deep convolutional neural networks," in *Advances in neural information processing systems*, 2012, pp. 1097–1105.
- [43] R. L. Wasserstein and N. A. Lazar, "The asa's statement on p-values: context, process, and purpose," 2016.
- [44] S. Kothari, J. H. Phan, and M. D. Wang, "Eliminating tissue-fold artifacts in histopathological whole-slide images for improved image-based prediction of cancer grade," *Journal of pathology informatics*, vol. 4, 2013.
- [45] Y. Gong and I. F. Sbalzarini, "A natural-scene gradient distribution prior and its application in light-microscopy image processing," *IEEE Journal of Selected Topics in Signal Processing*, vol. 10, no. 1, pp. 99–114, 2016.
- [46] —, "Curvature filters efficiently reduce certain variational energies," *IEEE Transactions on Image Processing*, vol. 26, no. 4, pp. 1786–1798, 2017.